LANGMUIR Article
Cite This: Langmuir 2019, 35, 13880−13892
pubs.acs.org/Langmuir

Structure and Dynamics of Spherical and Rodlike Alkyl Ethoxylate Surfactant Micelles Investigated Using NMR Relaxation and Atomistic Molecular Dynamics Simulations

Allison Talley Edwards,[†,‡] Abdolreza Javidialesaadi,[†,∥] Katie M. Weigandt,[§] George Stan,*[,†] and Charles D. Eads*[,‡]

[†]Department of Chemistry, University of Cincinnati, Cincinnati, Ohio 45221, United States
[‡]Corporate Research & Development, The Procter & Gamble Company, Mason, Ohio 45040, United States
[§]National Institute of Standards and Technology, 100 Bureau Drive, MS 6102, Gaithersburg, Maryland 20899, United States

Supporting Information

ABSTRACT: Predicting and controlling the properties of amphiphile aggregate mixtures require understanding the arrangements and dynamics of the constituent molecules. To explore these topics, we study molecular arrangements and dynamics in alkyl ethoxylate nonionic surfactant micelles by combining NMR relaxation measurements with large-scale atomistic molecular dynamics simulations. We calculate parameters that determine relaxation rates directly from simulated trajectories, without introducing specific functional forms to describe the dynamics. NMR relaxation rates, which depend on relative motions of interacting atom pairs, are influenced by wide distributions of dynamic time scales. We find that relative motions of neighboring atom pairs are rapid and liquidlike but are subject to structural constraints imposed by micelle morphology. Relative motions of distant atom pairs are slower than nearby atom pairs because changes in distances and angles are smaller when the moving atoms are further apart. Large numbers of atom pairs undergoing these slow relative motions contribute to predominantly negative cross-relaxation rates. For spherical micelles, but not for cylindrical micelles, cross-relaxation rates are positive only for surfactant tail atoms connected to the hydrophilic headgroup. This effect is related to the lower packing density of these atoms at the hydrophilic−hydrophobic boundary in spherical vs cylindrical arrangements, with correspondingly rapid and less constrained motion of atoms at the boundary.

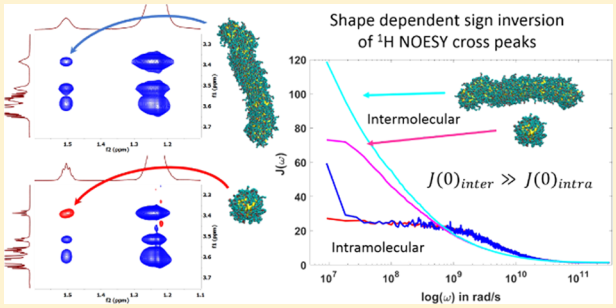

INTRODUCTION

Surfactant and amphiphile aggregates control or influence the properties of many materials relevant to biology, medicine, industry, technology, and more.[1−3] Specific examples of commercial application areas include consumer cleaning products, oil recovery,[4] and drug delivery.[5,6] Commercial mixture properties that depend on amphiphile aggregate structure and dynamics include viscosity,[7−10] foaming,[11] and the ability to suspend and deliver solubilized materials like flavors, fragrances,[12−15] and drugs.[16] Amphiphile aggregate-based materials are often empirically designed to create and exploit these properties.[12] However, small uncontrolled changes in composition or conditions can lead to large, unpredictable, and consequential property changes.[17−19]

Deeper understanding and better control of these properties can be gained by pursuing a detailed study of the arrangements and dynamics of molecules within the aggregates. Molecular dynamics (MD) simulations[20−23] and nuclear magnetic resonance (NMR) relaxation measurements[24,25] provide information of this nature, and these techniques are especially valuable when used together.[26−29] Combining experiments and simulations, bridged by theory, makes it possible to develop a detailed description of aggregate structure and dynamics and to refine our ability to interpret experimental results in related aggregate systems. Of the techniques available for studying aggregate dynamics, NMR is uniquely capable of measuring a vast range of molecular dynamics time scales ranging over 9 orders of magnitude.[30,31] NMR relaxation phenomena are particularly informative for exploring dynamics time scales ranging from picoseconds to microseconds.[27,32,33]

Numerous literature reports describe the structure and dynamics of aggregate structures utilizing MD simulations, NMR relaxation, or a combination of the two. These reports address structured biomacromolecules including proteins, nucleic acids, and complex carbohydrates and a variety of other materials including bulk liquids and amphiphile aggregates.[22,25,27,34−44] In some limiting situations, simple analytical expressions can be used to simplify the interpretation

Received: May 6, 2019
Revised: September 27, 2019
Published: October 1, 2019

DOI: 10.1021/acs.langmuir.9b01345
Langmuir 2019, 35, 13880−13892

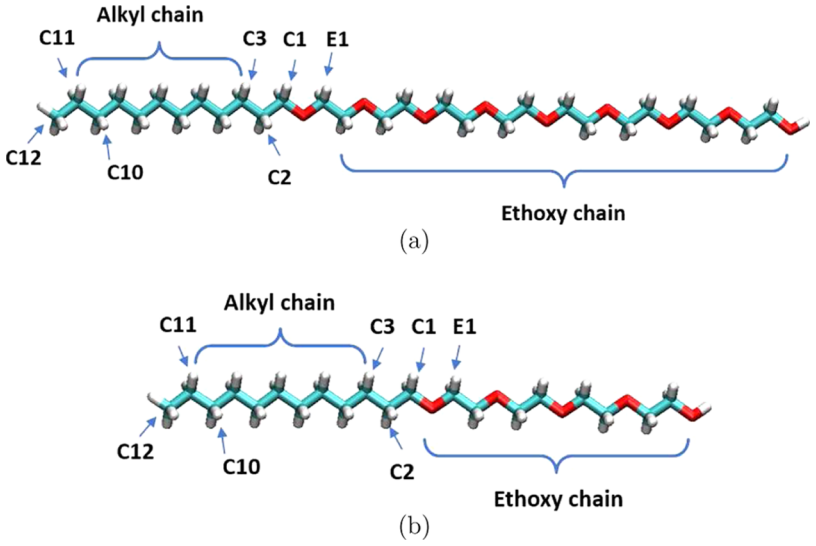

Figure 1. Molecular structure of (a) $C_{12}E_8$ and (b) $C_{12}E_4$ surfactants. Alkyl chain carbon atom numbering and ethoxy chain groups are indicated. Carbon atoms are designated with blue, oxygen atoms with red, and hydrogen atoms with white.

of simulations or to directly describe the dynamics. For example, great simplification arises when interatomic distances are approximately constant and different atoms are spectroscopically resolvable. This is often the case for isotropically tumbling organic molecules and for biomacromolecules.[37] In other cases, interatomic distances do not remain constant, and different atoms are not resolvable. This situation arises especially in systems consisting of bulk liquids or polymers. Such systems are often analyzed following Torrey[45] by using propagators to bridge molecular distribution functions with molecular dynamics to accommodate large networks of coupled, diffusing spins.[46,47]

Our aim in this work is to understand the structural and dynamic origins of NMR relaxation phenomena observed in nonionic surfactant micelles. We pursue this using a combination of experimental, computational, and theoretical approaches. Nonionic surfactants are widely used and versatile in applications and make excellent model systems for experiment and theory.[48−51] While the study of nonionic micelle structure and dynamics has a long history, dynamic aspects of the aggregates are still insufficiently understood.[25,52−56] For example, experimental measurements shown in this work of cross-relaxation in these micelles using two-dimensional ^{1}H-^{1}H Nuclear Overhauser Effect SpectroscopY (NOESY) give mostly negative cross-relaxation rates, which typically accompany slow molecular motions. However, alkyl chain protons adjacent to the ethoxy headgroup exhibit positive cross-relaxation rate constants in some of these systems, indicative of rapid molecular motions. Notably, these protons are located at the boundary between hydrophobic and hydrophilic regions of spherical micelles, where we might expect atoms to be especially sterically constrained and dynamically encumbered by the structure of the micelle.[39,57,58]

To obtain microscopic-level understanding of phenomena revealed by these NMR experiments, we perform extensive atomistic MD simulations that sample a total of ≃2.7 μs. We then analyze the results in the context of the NMR relaxation theory. Rather than relying on analytical models or their underlying assumptions, we consult MD trajectories directly to obtain insights into the relaxation behavior. To inform interpretation of NMR relaxation phenomena, simulations must adequately sample dynamics over a correspondingly large range of time scales. Doing so suggests an explanation of the observed relaxation behavior. This enables a deeper understanding of structure and dynamics in amphiphile aggregates and improves our ability to gain information from these techniques.

METHODS

Experimental. Samples contained nonionic alkyl ethoxylate surfactants of type C_iE_j, where i denotes the number of carbon atoms in the alkyl chain and j is the number of ethoxy units. Octaethylene glycol monododecyl ether ($C_{12}E_8$), hexaethylene glycol monododecyl ether ($C_{12}E_6$), tetraethylene glycol monododecyl ether ($C_{12}E_4$), and deuterium oxide (D_2O) were purchased from Sigma-Aldrich and used without further purification. The surfactants were combined with pure D_2O and allowed to equilibrate for 24 h at room temperature before data acquisition. One series of samples was created to probe micelle shapes from spherical to increasingly long wormlike structures. For this series, samples were prepared having relative (molar) amounts of $C_{12}E_8$ and $C_{12}E_4$ of 1:0, 3:1, 2:1, and 1:1. The total surfactant concentration in these samples was 80 mM in every case. Another sample was prepared to study relaxation rates across a thermally driven transition from a hexagonal phase to a micellar phase. This sample contained $C_{12}E_6$ at 50% wt/wt in D_2O.

All ^{1}H relaxation measurements were performed with vendor-supplied pulse sequences using a Bruker Avance III 600 MHz instrument, while ^{13}C relaxation measurements were performed using a Bruker Avance 700 MHz instrument. The two-dimensional ^{1}H-^{1}H Nuclear Overhauser Effect SpectroscopY (NOESY) technique was used to measure cross-relaxation using the pulse sequence noesygpphpp. The mixing time was 400 ms, and the data were acquired with 4096 points in F2, 1024 points in F1, and using a relaxation delay of 10 s. One-dimensional ^{1}H spectra were collected with the zg pulse sequence using 16 scans and an interscan relaxation delay of 20 s. ^{1}H T_1 and ^{13}C T_1 data were acquired using the t1ir and t1irpg pulse sequences, respectively, using 16 time increments and an interscan relaxation delay of 55 s. ^{1}H T_2 measurements were performed using the cpmg pulse sequence with an interscan relaxation delay of 55 s. Unless otherwise specified, all experiments were performed at 25 °C. To monitor the thermally driven phase transition, NOESY spectra were acquired at 25, 35, 40, and 45 °C as described above.

Molecular Dynamics Simulations. We perform all-atom simulations of a spherical micelle comprising pure $C_{12}E_8$ and of a

DOI: 10.1021/acs.langmuir.9b01345
Langmuir 2019, 35, 13880−13892

cylindrical micelle comprising a 1:1 mixture of $C_{12}E_8$ and $C_{12}E_4$. As the reported range of aggregation numbers for $C_{12}E_8$ at 25 °C range from 80 to 120,[59−62] we choose an aggregation number of 99. The resulting micelles have an average radius of 29.5 Å. Aggregation numbers of extended wormlike micelles of the type C_iE_j are reported to be ≥1000,[10,54] which would require atomistic simulations that are computationally too demanding. Therefore, we study cylindrical micelles with lower aggregation numbers that reproduce an aggregate with a contour length larger than the 150−200 Å persistence length of C_iE_j nonionic micelles.[63] To this end, we consider cylindrical micelles comprising 400 $C_{12}E_8$ and 400 $C_{12}E_4$ molecules, which have an average contour length ≃320 Å and a cross-sectional radius ≃24 Å. Models of aggregate structures are obtained using the Packmol[64] software package. For spherical micelles, we arrange 99 of the linear molecules of $C_{12}E_8$, shown in Figure 1, in an initial spherical shape using a distance tolerance of 2.0 Å. These structures are then solvated using 36783 TIP3P water molecules in a rhombic dodecahedron box with dimensions 120 Å × 120 Å × 120 Å, corresponding to a total of 119 754 atoms. The cylindrical micelle comprises 400 $C_{12}E_8$ and 400 $C_{12}E_4$ molecules each, shown in Figure 1. These are then arranged in a cylindrical shape with a tolerance of 2.0 Å. To facilitate faster solvation and equilibration, this structure is first minimized using the conjugate gradient method for 500 steps. Next, the minimized structure is solvated using 173 866 TIP3P water molecules in an orthorhombic box with dimensions 130 Å × 130 Å × 350 Å, corresponding to a total of 586 398 atoms.

MD simulations are performed using the molecular modeling program NAMD version 2.12[65] and the CHARMM36 force field.[66,67] Interactions involving surfactant molecules are modeled using the standard CHARMM36 parameters including the ethers parameter set, and interactions involving water molecules are modeled using the TIP3P parameter set. The force field and water model used here were shown to yield accurate size and shape properties of micelles.[21,58,68−71] Periodic boundary conditions are applied, and electrostatic interactions are treated using particle mesh Ewald[72] with a grid spacing of 1 Å. The integration algorithm uses the velocity Verlet method with an integration time step of 2 fs. Nonbonded interactions are truncated using a switching function between 10 and 12 Å. All covalent bond lengths involving hydrogen are held constant using the SHAKE algorithm[73] with a tolerance of 1.0×10^{-8} Å. The pressure and temperature are controlled with a Nosé−Hoover Langevin piston using a reference pressure of 1 bar and damping coefficient of 2 ps^{-1}. Simulations are performed at T = 300 K.

For both spherical and cylindrical systems, the initial solvated Packmol model structures are energy minimized using the conjugate gradient method for 5000 steps. Next, equilibration simulations at T = 300 K are performed for 10 ns with the spherical micelles and for 50 ns with the cylindrical micelles. Equilibration is attained when stable radius of gyration (R_g) and eccentricity (e) values are reached. The eccentricity is defined as $e = 1 - I_{min}/I_{avg}$, where I_{min} and I_{avg} are the smallest and the average principal moment of inertia, respectively.[74] We find that $e \simeq 0.10 \pm 0.04$ for spherical micelles and $e \simeq 0.85 \pm 0.01$ for cylindrical micelles. These values are consistent with spherical and cylindrical shapes, respectively, considering the limiting cases of a perfect sphere (e = 0) and of an infinitely long rod (e = 1). The equilibrium value of R_g for spherical micelles is ≃23.7 ± 0.1 Å and for cylindrical micelles it is ≃85.0 ± 1.6 Å. The configurations obtained after these equilibration simulations were used as initial configurations of production runs. One additional configuration was obtained for each of the micelle types by extending the equilibration simulations for 20 ns. Representative structures are shown in Figure 2a,b with water omitted for clarity. Two production trajectories are performed for each micelle for 680 ns and are sampled at 10 ps intervals to capture frequencies up to 100 times faster than the Larmor frequency at 14.1 T (600 MHz). As MD simulations have a finite duration of 680 ns, they provide no information on dynamic processes with longer time scales.

Calculating NMR Relaxation Rates from Simulations. *Synopsis of the Relaxation Theory.* The relaxation theory used in this work has been summarized in standard references.[75−78] In short,

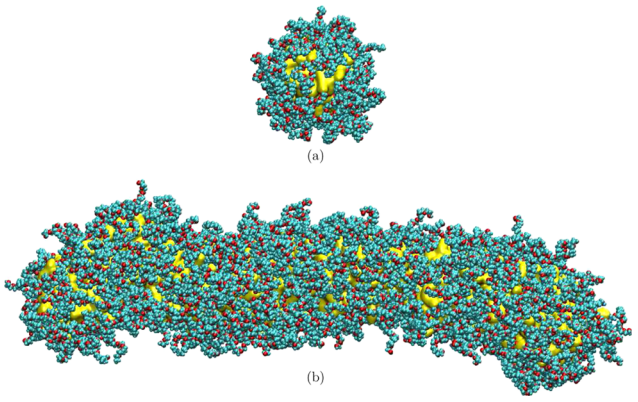

Figure 2. Equilibrated micelle structures: (a) $C_{12}E_8$ spherical micelle and (b) 1:1 molar ratio $C_{12}E_8/C_{12}E_4$ cylindrical micelle. The alkyl core is shown in yellow, the methylene units of the ethoxy headgroups are shown in cyan, and the oxygen atoms are shown in red. Water molecules are omitted for clarity.

according to the Bloembergen, Purcell, and Pound (BPP) perturbation theory, nuclear spin relaxation rates are functions of spin state transition probabilities.[79] These transition probabilities are, in turn, proportional to the intensities of fluctuations in interactions that occur at frequencies that match differences between the energy levels of spin systems. Spectral density functions $J(\omega)$ quantify these intensities and are determined by the Fourier transformation of correlation functions $G(\tau)$ that characterize the time dependence of the interactions underlying the relaxation. Relaxation processes studied in this work are dominated by fluctuations in the magnetic dipole−dipole coupling among pairs of nuclei. Given reliable trajectories, the main task in relating MD simulations to NMR relaxation phenomena is therefore to calculate correlation functions for the dipole−dipole interactions from the trajectories.

Because of the algebraic form of the dipole−dipole interaction, magnetic dipole−dipole correlation functions can be expressed in terms of second-rank spherical harmonics and the internuclear distances as

$$G(\tau) = \sum_{m=-2}^{2} G_m(\tau) = \sum_{m=-2}^{2} K_{IS} \left\langle \frac{(Y_2^m(\theta(t), \phi(t)))^*}{r^3(t)} \frac{Y_2^m(\theta(t+\tau), \phi(t+\tau))}{r^3(t+\tau)} \right\rangle \quad (1)$$

where $r(t)$ is the distance between the two interacting nuclei, $Y_2^m(\theta(t),\phi(t))$ are the spherical harmonics, and $\theta(t)$ and $\phi(t)$ are the polar and azimuthal angles in the laboratory frame with the applied magnetic field defining the polar axis. K_{IS} contains physical constants related to the magnetic properties of the insensitive (I) and sensitive (S) interacting spins, $K_{IS} = \left(\frac{\mu_0}{4\pi}\hbar\gamma_I\gamma_S\right)^2$, where μ_0 is the vacuum permittivity, $\hbar$ is the Planck constant divided by 2π, and γ is the gyromagnetic ratio.

Inspection of eq 1 indicates that correlation functions calculated from MD simulation trajectories depend on changes in orientation, reflected in spherical harmonic terms of all orders m, and on changes in the distances between nuclei. For cases where internuclear distances are approximately constant, for example, ^{13}C relaxation, which is dominated by directly attached hydrogen atoms, analysis can be simplified by separating the distance and angle variables. For cases where the internuclear distances vary, for example, when the interacting nuclei reside on different molecules, such simplifications are not valid since it is necessary to accommodate the distance fluctuations and potential correlations between distance and angle fluctuations.[46,47] We note that the correlation function $G(\tau)$ may be expressed in a compact form by using the second-order Legendre

DOI: 10.1021/acs.langmuir.9b01345
Langmuir 2019, 35, 13880−13892

polynomial, P_2, to represent the angular part via the addition theorem[33,37] $P_2(\cos\chi_{t,t+\tau}) = (4\pi/5)\sum_{m=-2}^{2}(Y_2^m(\theta(t),\phi(t)))^*Y_2^m(\theta(t+\tau),\phi(t+\tau))$, where $\chi_{t,\,t+\tau}$ is the angle of the internuclear vector at t and $t+\tau$.

Because correlation functions are even and real, Fourier transformation is equivalent to real-valued cosine transformation of the correlation function to generate the spectral density function

$$J_m(\omega) = 2\int_0^\infty G_m(\tau)\cos(\omega\tau)\mathrm{d}\tau \tag{2}$$

Given the spectral density functions, the relaxation rates due to proton−proton dipolar coupling are given by

$$\frac{1}{T_1} = J_1(\omega_H) + 4J_2(2\omega_H) \tag{3}$$

$$\frac{1}{T_2} = \frac{3}{2}J_0(0) + \frac{5}{2}J_1(\omega_H) + J_2(2\omega_H) \tag{4}$$

$$\sigma = 6J_2(2\omega_H) - J_0(0) \tag{5}$$

Here, T_1 is the longitudinal relaxation time, T_2 is the transverse relaxation time, and σ is the cross-relaxation rate. ω_H is the Larmor frequency of protons for the magnetic field used in the experiment, 600 MHz in this work.

The expression for ^{13}C T_1 due to carbon−proton dipolar coupling is

$$\frac{1}{T_1} = \frac{N}{4}(J_0(\omega_H - \omega_C) + 3J_1(\omega_C) + 6J_2(\omega_H + \omega_C)) \tag{6}$$

where N is the number of protons attached to the carbon atom, and the Larmor frequency of carbon is ω_C. ^{13}C relaxation measurements are performed on a 16.4 T instrument, so ω_C is 176 MHz and ω_H is 700 MHz.

Treatment of Rigid-Body vs Internal Motion Contributions. Properties of globular proteins and amphiphile aggregate systems may be examined by highlighting contributions of rigid-body (overall) and internal dynamics on different time scales.[34,35,40,80,81] In the context of protein relaxation analysis, Ollila et al.[80] developed a sophisticated analysis of anisotropic diffusion to obtain an effective correlation time for rigid-body rotational diffusion, which provides the dominant contribution to correlation functions. Néry et al.[35] utilized the two-step[82] and three-step models to describe experimental ^{13}C relaxation in spherical and nonspherical micelles. A satisfactory account of the data was achieved by assuming that the rotational tumbling of the micelle and lateral surfactant diffusion together account for the long correlation times in the model. Interestingly, they conclude that the lateral diffusion of the amphiphiles dominates the long correlation times in both spherical and nonspherical micelles. Bogusz et al.[40] identify complex liquidlike motions of individual amphiphiles within a nonionic micelle that are not readily separable and that render a rigid sphere model inadequate. For nonionic amphiphilic bilayers, Ferreira et al.[43] used separation of rigid-body and internal dynamics contributions to the correlation function along with a novel experimental scheme to disentangle rigid-body and internal motion time scales. Klauda et al.[81] analyzed the relative contribution of motions of individual lipid molecules within a lipid bilayer. Overall, for aggregates such as globular proteins that have restricted internal motions, rigid-body rotational and translational motions often dominate the correlation functions. By contrast, surfactant and lipid aggregates have internal diffusive motions of the amphiphiles that may lead to more rapid decay of correlation functions.[27,40,81]

Our perspective is to work as directly as possible with the correlation functions that emerge from direct analysis of the simulated trajectories. We do not attempt to separate rigid-body motions from internal motions, and we do not attempt to separately analyze fluctuations in distances and angles. To that end, we calculate correlation functions for all orders of the spherical harmonics and for all distances, and we average these to obtain effective correlation functions for use in eqs 3−5. This approach leads to spectral density functions having less noise, makes no significant difference in calculated relaxation parameters compared with the more rigorous treatment, and facilitates analysis and discussion.

Calculation of Spectral Density Functions without Fitting to an Analytic Expression. Correlation functions calculated from MD trajectories are typically noisy and unsuited for direct conversion to spectral density functions. They are therefore traditionally fit to a functional form, usually a sum of exponential functions, to generate a parametrized algebraic expression. The resulting correlation function is then subjected to symbolic Fourier transformation to generate the spectral density function. In this work, for analysis of cross-relaxation, we do not need to assume a functional form for the correlation function because of the extensive averaging achieved using the long simulations. Instead, we calculate the spectral density function by Fourier transformation of the correlation functions obtained directly from the simulations.

The critical advantage of this approach is that it does not depend on any assumptions or model of the dynamics. A disadvantage is that the lowest frequency available in the resulting spectral density function is limited by the duration of the simulation since our correlation functions do not always fully decay within that time. Without a functional form, we have no basis for extrapolation. Low-frequency motions are especially important for predicting cross-relaxation rates, which are strongly influenced by the (near) zero-frequency spectral density. Our approach allows calculation of a lower limit on this low-frequency spectral density, but it does not provide a basis for extrapolation beyond that limit. We are therefore not able to make numerical estimates of cross-relaxation rates, but based on the lower limits, we are able to draw qualitative conclusions.

Correlation Functions Involving Multiple Unresolvable Coupling Partners. Equations 1 and 2 apply to individual spin pairs, whereas micelles have numerous spectroscopically indistinguishable nuclei at many different distances that contribute in an additive manner to the measured relaxation rates. Even though the effect of dipole−dipole coupling falls off rapidly with distance (as r^{-6}), there are many spins at long distances whose cumulative effects are significant.[46] For example, consider a smooth isotropic distribution whose closest internuclear distance is r_{min}. Integrating over all space gives $\langle r^{-6}\rangle = (4\pi/3)r_{min}^{-3}$, which is longer range in distance by a power of three. Distributions in amphiphile aggregates are not smooth, isotropic, or infinite, but this shows that distant spins can be important and will play an important role in the discussion below.

To account for the long-range contributions in micelles, interactions must be added and averaged appropriately,[83] so we use the following procedure. We consider groups of spins that, within a group, may be spectroscopically unresolvable. Considering a single reference spin of group l, we make a list of all spins of another group k that, at some point along the simulated trajectory, appears within the cutoff distance of 10 Å of the type-l spin. For every k spin so identified, the correlation function with the reference spin of type l is computed using eq 1, including contributions from time steps when the distance exceeds the cutoff distance. We then sum all correlation functions generated by this list, separating intramolecular and intermolecular correlations. We repeat this process for a definite number of spins and then average these correlation functions to generate an average correlation function for l,k spin pairs. We find that averaging the results of this procedure over 99 spins of group l gives a reasonable compromise of computation time and adequate sampling.

Defining Dynamic Time Scales Using Spectral Density Functions Involving a Single Exponential Correlation Function. Though we calculate spectral density functions directly from MD trajectories, insights into expected behavior, and some common vocabulary, come from consideration of simple models. In particular, the conventional distinction between fast and slow motions arises from the single exponential case. We use this terminology throughout. The model assumes that the rotational correlation function decays monoexponentially

$$g(\tau) = \exp\left(-\frac{t}{\tau_c}\right) \tag{7}$$

DOI: 10.1021/acs.langmuir.9b01345
Langmuir 2019, 35, 13880−13892

and that the rotational correlation time τ_c characterizing this function is the same as the tumbling time of the relaxing molecule or aggregate. In this case, the spectral density function is given by

$$j(\omega) = \frac{\tau_c}{1 + \omega^2\tau_c^2} \quad (8)$$

(We use lower-case symbols for correlation and spectral density functions to indicate that we drop physical and numeric factors to simplify notation.)

When τ_c is short so that $\omega\tau_c \ll 1$, the process is deemed fast, and the spectral density is proportional to τ_c. When τ_c is long so that $\omega\tau_c \gg 1$, the process is deemed slow, and the spectral density function is proportional to $(\omega^2\tau_c)^{-1}$. In the following, we use the terms fast and slow in relation to time scales relative to the spectrometer frequency.

Small-Angle Neutron Scattering (SANS) Methods. Samples prepared for small-angle neutron scattering (SANS) contained 4 mM $C_{12}E_8$ or a mixture of 2 mM $C_{12}E_8$ and 2 mM $C_{12}E_4$ in D_2O. Additional samples were prepared to ensure that the sample was sufficiently dilute to neglect interactions between particles. All SANS measurements were performed on the NGB 10 m beamline at the NIST Center for Neutron Research. Three configurations using 5 or 12 Å neutrons were used to access a q range from 0.004 to 0.6 $Å^{-1}$, which resolves structures from 10 to 1500 Å. The scattering curves were corrected for background and reduced to absolute scale using the standard NIST reduction IGOR macros.[84]

RESULTS AND DISCUSSION

Micelle Shape and Size. To interpret the relaxation behavior and to properly perform the MD simulations, it is necessary to describe the micelle morphology. We characterize the simulated and measured systems using small-angle neutron scattering as described above. As shown in Figure 3, for the pure $C_{12}E_8$ sample, we observe a transition from a Porod slope, $I \propto q^{-4}$, at high q values to a Guinier plateau, $I \propto q^0$, at low q, which is consistent with a spherical form factor. For the mixed surfactant sample, there is an additional intermediate Guinier region where $I \sim q^{-1}$, which is a characteristic scattering feature of an extended linear or cylindrical morphology. To further characterize the morphology of the micelles, the scattering data were fit using form factor models for spherical and cylindrical objects[85,86] using SASView,[87] and the radius and length (for the cylindrical micelles) were determined, as reported in the caption to Figure 3.

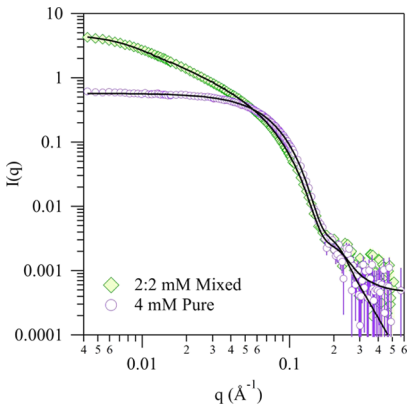

Figure 3. Shape determination of $C_{12}E_8$ and 1:1 $C_{12}E_8/C_{12}E_4$ micelles via small-angle neutron scattering. The pure $C_{12}E_8$ micelle data (here designated as pure, denoted in purple circles) fits to a sphere model with a radius of 24.5 ± 0.2 Å. The mixed 1:1 molar ratio $C_{12}E_8/C_{12}E_4$ micelle (here designated as mixed, denoted in green shaded diamonds) fits to a cylinder model with a radius of 21.4 ± 0.3 Å and length of 518 ± 3 Å. Fits are shown in black. (See text for details of the fitting procedure.) Standard errors larger than the size of the circles are indicated through error bars.

Cross-Relaxation, Longitudinal Relaxation, and Transverse Relaxation in Spherical and Cylindrical Micelles. In this section, we present relaxation data acquired to explore motions that occur in C_iE_j micelles. The different relaxation processes in eqs 3−6 are sensitive to different aspects of structure and dynamics. They are controlled by dynamics at different frequencies and by the identities of atoms that contribute to the processes.

Cross-relaxation rates, as measured via the two-dimensional NOESY method, are especially informative because they can be ascribed to specific pairs of resolvable groups of atoms, making interpretation easier.[88] Cross-relaxation rates are also valuable because they exhibit qualitative differences, being either negative or positive, depending on differences in spectral densities at frequencies of zero and $2\omega_0$ (eq 5), thereby reporting on a wide range of dynamic time scales. Comparing longitudinal (T_1) and transverse (T_2) ^{1}H relaxation times is also valuable though they have nonspecific contributions from all pairs of interacting ^{1}H atoms. According to eqs 3 and 4, when motions are fast, the two relaxation times are equal. When large zero-frequency spectral density components are present, T_2 becomes shorter than T_1. ^{13}C T_1 relaxation times (eq 6) are informative because they depend exclusively on local motions. At the low natural abundance of the ^{13}C isotope, only the covalently bonded hydrogen nuclei contribute measurably to relaxation. Slow motions are relatively irrelevant to ^{13}C T_1 relaxation when rapid motions are also present.

Figure 4 shows a contour plot of a key region of the two-dimensional NOESY spectrum (see full NOESY spectra in the Supporting Information Figures S1 and S2). It exhibits several of the features explored in this work. To a first approximation,

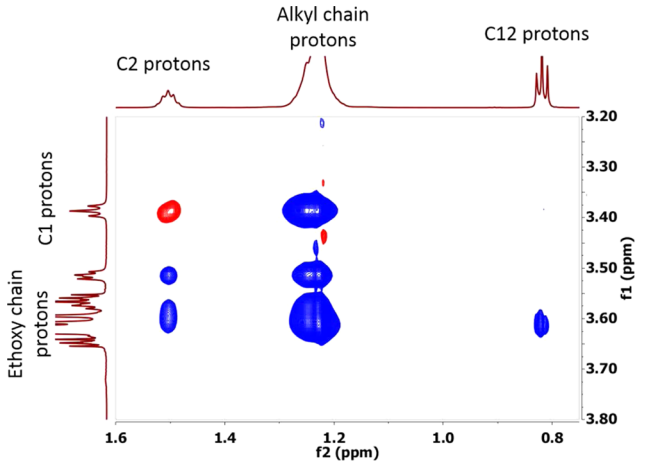

Figure 4. Region of the ^{1}H-^{1}H NOESY spectrum of 80 mM $C_{12}E_8$ in D_2O at 25 °C showing cross-peaks between ethoxy chain protons, C1 protons, C2 protons, alkyl chain protons, and terminal methyl C12 protons (for carbon numbering convention, refer to Figure 1). Chemical shifts relevant to the cross-peaks are identified in the one-dimensional ^{1}H spectra displayed along the axes of the figure. Pairs of nuclei involved in cross-relaxation appear as peaks in a NOESY spectrum. Negative and positive signals are distinguished using blue and red contour lines, respectively. The negative sign of cross-peaks indicates that slow motions dominate the cross-relaxation process, while the positive 1−2 cross-peak indicates that rapid motions dominate the cross-relaxation process.

DOI: 10.1021/acs.langmuir.9b01345
Langmuir 2019, 35, 13880−13892

signals in NOESY spectra are proportional to signed cross-relaxation rates (eq 5) and to the populations of the coupled spin groups. Negative and positive signals are shown in blue and red, respectively.

For the spherical $C_{12}E_8$ micelles, all but one of the cross-relaxation rates are negative. The important exception is the peak due to interactions between hydrogen atoms on carbon atoms 1 and 2. According to eq 5, negative or positive cross-relaxation rates correspond to slow and fast modulations, respectively, of the dipole−dipole interactions leading to cross-relaxation. In the case of spherical micelles, cross-relaxation between atoms at positions 1 and 2 is dominated by fast motions, whereas for the cylindrical micelles, the cross-relaxation is dominated by slow motions.

Table 1 shows experimental ^{1}H T_1 and ^{1}H T_2 values for several signals. In all cases, T_1 values are longer than T_2 values.

Table 1. ^{1}H T_1 and T_2 Values Calculated from Experiment[a]

proton	spherical T_1 (ms)	spherical T_2 (ms)	cylindrical T_1 (ms)	cylindrical T_2 (ms)
E1	625	237	603	89
C1	632	96	617	27
C2	598	71	603	20
C3−C11	718	142	711	32
C12	1390	249	1110	119

[a]Proton designation follows the five resolvable ^{1}H peaks and is denoted by the heavy atom to which it is attached, starting at the carbon on the ethoxy unit directly adjacent to the alkyl chain (E1). Protons on C1 and C2 are distinguishable, while protons on the main alkyl chain from carbon 3 to carbon 11 are contained in a single broad peak. The terminal methyl protons are resolvable and denoted C12. Relaxation rates for 80 mM $C_{12}E_8$ (spherical) micelles and 80 mM total surfactant 1:1 molar ratio of $C_{12}E_8/C_{12}E_4$ (cylindrical) micelles were determined on a Bruker 600 MHz (14.1 T) magnet utilizing the t1ir and cpmg pulse sequences. Samples were solvated in D_2O. Experimental samples were analyzed at 298 K. Experimental error is less than 10%.

This shows that the correlation functions throughout have slowly decaying components, leading to significant zero-frequency spectral densities. This contrasts with results for small unconstrained molecules without slowly decaying components, where T_1 and T_2 are typically equal. Starting with position 2 in the hydrophobic tails, the relaxation times become longer toward the CH_3 chain terminus, suggesting that motions become faster along the chain in this dimension. Relaxation times at position 1 are longer than at position 2, indicating faster motions at the hydrophobic−hydrophilic interface of the aggregates. T_1 values for spherical and cylindrical micelles are nearly identical for corresponding positions. This indicates that spectral densities at ω and 2ω are very similar in the two cases. On the other hand, T_2 values in spherical micelles are systematically longer than in cylindrical micelles at the same positions. This indicates that zero-frequency spectral densities (and therefore slower motions) are relatively more prevalent in cylindrical vs spherical micelles.

Unlike the cross-relaxation data, however, there is no qualitative difference between T_1 and T_2 values for atoms near the surfactant headgroups in spherical vs cylindrical micelles. ^{1}H T_1 and T_2 values for a particular nucleus depend on a sum of contributions from all nuclei that interact with that nucleus. Cross-relaxation, on the other hand, depends only on interactions between specific pairs of nuclei. In addition, because the signs of contributions from fast and slow motions are different, the cross-relaxation rate can differ qualitatively depending on the dominant time scale of specific internuclear interactions. Because of this lack of specificity provided by ^{1}H T_1 and T_2 values, and the fact that differences between T_1 and T_2 for the two micelle types do not help explain the cross-relaxation rate sign change results, we do not focus on calculating ^{1}H T_1 and T_2 values via simulations in this work.

Figure 5a,b shows that the sign and intensity of the C1−C2 cross-peak can be systematically manipulated by changing the composition or conditions, and consequently the shape, of $C_{12}E_j$ surfactant aggregates. Figure 5 shows that by adjusting the composition of the micelles to cause a shape transition from wormlike to spherical, the 1−2 cross-peak changes sign from negative to positive. Figure 5 shows that for a thermally driven phase transition from a hexagonal to micellar phase, the 1−2 cross-peak also changes sign from negative to positive.[89]

Table 2 shows measured and simulated ^{13}C T_1 relaxation rates for selected resolvable signals in spherical and wormlike aggregates, indicating very good agreement between the experimental results and those calculated from simulation. While the TIP3P water model is known to predict lower water viscosities, this has only a weak effect in calculations involving surfactant tail carbons in micelles.[40] As water penetration to the micelle core is low and the contribution of the internal relaxation dynamics of individual spins dominates over the rigid-body rotation for solutes with high internal mobility (e.g., micelles or lipid bilayers),[37,40,80] correlation times of surfactant tails primarily reflect the accuracy of the hydrocarbon parametrization rather than the water model.[39,40] As discussed in the Methods, section, slow motion micellar ^{13}C T_1 NMR relaxation dynamics are dominated by internal diffusive motions,[35] which are relatively insensitive to aggregate shape. This leads to a reduction of the effect of the viscosity of the water model on surfactant tail relaxation values in micelles. In either case, both experimental and simulated relaxation times increase (relaxation rates decrease) systematically along the alkyl chain, a trend that normally indicates that the mobility increases.

According to these data, in both the spherical and cylindrical micelles, the least mobile atoms reside at the boundary between hydrophobic and hydrophilic regions of the aggregates. Assuming a single correlation time, and in light of eq 6, we find correlation times ranging from $\sim 7 \times 10^{-12}$ s for position 1 to $\sim 1 \times 10^{-12}$ s for position 12. These correlation times are liquidlike, in the sense that relaxation measurements on neat liquid hydrocarbons of comparable size give correlation times of similar magnitudes. The simulated relaxation times in Table 2 will be discussed below.

Morphology-Dependent Molecular Packing and Dynamics Underlie the Behavior of Cross-Relaxation Rates in Micelles. The emphasis on the analysis of simulated MD in this report is to address several key features of these experimental results. Cross-relaxation rates σ are predominately negative. This suggests, via eq 5, that slow motions usually dominate cross-relaxation. Cross-relaxation involving positions 1 and 2 indicates fast motions at the hydrophobic−hydrophilic boundary for spherical micelles, and slow motions otherwise. ^{1}H T_1 and T_2 results also support the importance of slow motions, though somewhat less specifically than the NOESY results. ^{13}C T_1 results suggest, via eq 6, that internal micelle motions occur on fast liquidlike time scales, but they are the slowest near the hydrophobic−hydrophilic boundary

DOI: 10.1021/acs.langmuir.9b01345
Langmuir 2019, 35, 13880−13892

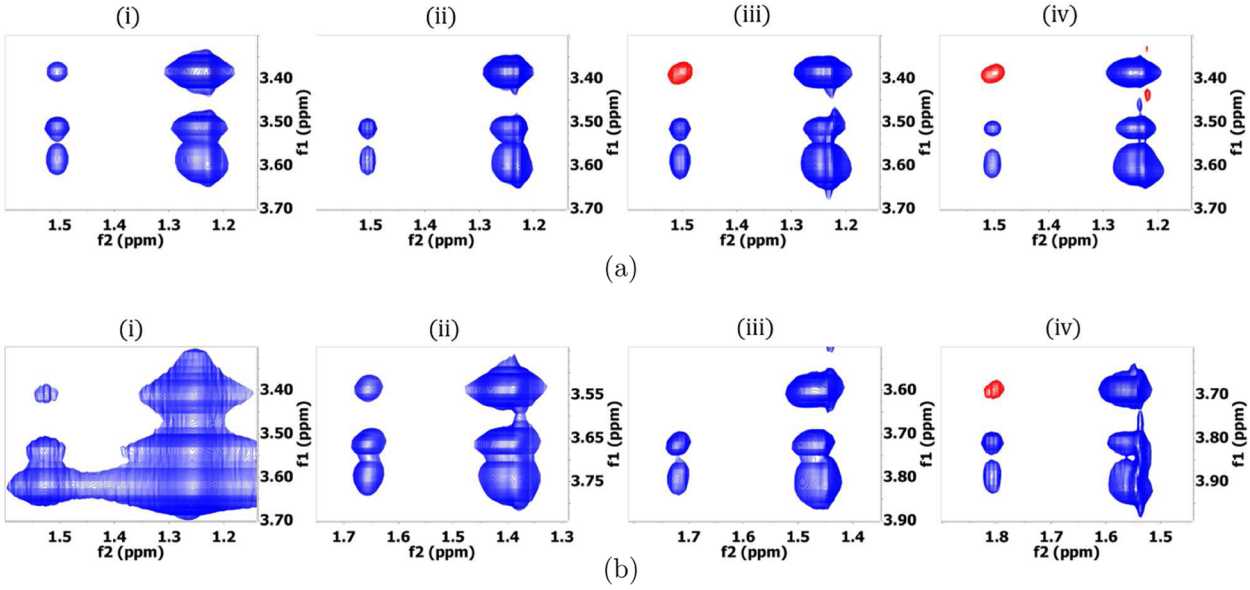

Figure 5. Illustration of the relation between micelle morphology and NOESY cross-peak signs. (a): NOESY cross-peaks among ethoxy chain protons, protons at positions 1 and 2, and unresolvable protons within the alkyl chains as a function of composition at 25 °C. Compositions shown are molar ratios of (i) 1:1, (ii) 2:1, (iii) 3:1, and (iv) 1:0 $C_{12}E_8/C_{12}E_4$. Total surfactant concentration is 80 mM in D_2O. (b) NOESY cross-peaks among ethoxy chain protons, protons at positions 1 and 2, and unresolvable protons within the alkyl chains as a function of temperature for 50% wt/wt $C_{12}E_6$ in D_2O. (i) is at 25 °C, (ii) is at 35 °C, (iii) is at 40 °C, and (iv) is at 45 °C.

Table 2. ^{13}C T_1 Values Calculated from Experiment and Simulation[a]

carbon	spherical T_1 (s) experiment	spherical T_1 (s) simulation	cylindrical T_1 (s) experiment	cylindrical T_1 (s) simulation
C1	0.65	0.60	0.67	0.55
C2	0.74	0.64	0.76	0.61
C3	0.72	0.74	0.77	0.73
C11	1.74	1.64	1.91	1.98
C12	2.85	2.47	2.88	2.56

[a]Relaxation rates for 80 mM $C_{12}E_8$ (spherical) micelles and 80 mM total surfactant 1:1 molar ratio of $C_{12}E_8/C_{12}E_4$ (cylindrical) micelles were determined on a Bruker 700 MHz (16.4 T) magnet utilizing the inversion-recovery method at 298 K in a D_2O solvent. Simulations were performed at 300 K. See text for details of calculations. Experimental and simulation errors are less than 10%.

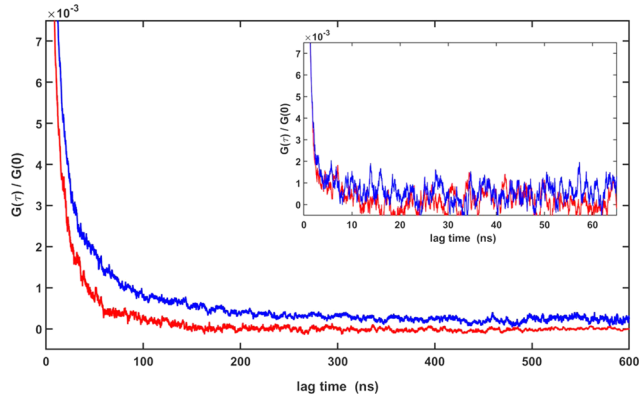

Figure 6. Normalized correlation functions $G(\tau)/G(0)$ for dipole−dipole interactions between protons located on carbons 1 and 2. Spherical micelles are shown in red, and cylindrical micelles are shown in blue. Main figure: correlation functions for intermolecular interactions. Inset: correlation functions for intramolecular interactions. Note the difference in the *x*-axis scale, which emphasizes that intermolecular interactions decay relatively slowly compared with intramolecular interactions. In addition, intermolecular interactions decay much more slowly for cylindrical vs spherical micelles, consistent with differences in spectral density functions suggested by cross-relaxation rates.

region of the aggregates. These relaxation results cannot all be explained using a simple dynamic model, such as that given in eqs 7 and 8, so a detailed exploration of dynamics in light of these experimental results is performed.

Dynamic Analysis of the C1−C2 Interaction. Figure 6 shows the normalized correlation functions for modulations of the dipole−dipole interactions between hydrogen atoms at positions 1 and 2. These were calculated from the MD simulations as described above. Intramolecular interaction dynamics appear very similar in the cylindrical and spherical micelles, and in both cases the correlation functions decay quickly. Correlation functions for intermolecular interactions have slow components in both cases, but behave differently in spherical compared with cylindrical micelles. Specifically, the intermolecular correlation function decays more slowly in the cylindrical vs the spherical case.

The relative contributions of intermolecular vs intramolecular interactions to the total interaction are controlled by the initial values of the correlation functions, $G(0)_{inter}$ and $G(0)_{intra}$, respectively. This follows from the properties of autocorrelation functions where $G(0)$ is the mean-square amplitude of the correlated function.[77,78] Intramolecular $G(0)_{intra}$ values were nearly identical in both micelle systems, while intermolecular $G(0)_{inter}$ values were found to be an order of magnitude lower. The plots of the correlation functions show that the motions must be described using a wide range of time scales. In the absence of an analytical formula that describes these correlation functions, we cannot parametrize the results to obtain analytical expressions for the spectral density functions. However, using long simulations and

DOI: 10.1021/acs.langmuir.9b01345
Langmuir 2019, 35, 13880−13892

extensive averaging, it is possible to calculate spectral density functions by direct Fourier transformation of the correlation functions as described above.

Figure 7 shows the resulting spectral density functions for hydrogen atoms at positions 1 and 2, corresponding to the

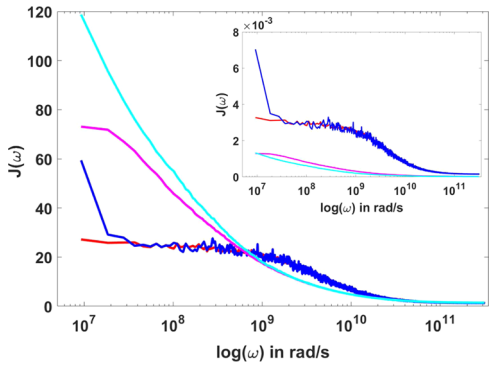

Figure 7. Spectral density functions from the Fourier transformation of correlation functions for dipole−dipole interactions between protons located on carbons 1 and 2. Main figure: normalized correlation functions $G(\tau)/G(0)$; inset: non-normalized correlation functions $G(\tau)$ multiplied by K_{IS}. Intramolecular spectral densities for spherical micelles are shown in red, and cylindrical micelles are shown in blue. Intermolecular spectral densities for spherical micelles are shown in magenta, and cylindrical micelles are shown in cyan. Our procedure does not allow extrapolation to zero frequency, so the low-frequency values represent lower limits on the zero-frequency spectral densities.

NOESY cross-peak that changes sign in Figure 5a,b. The correlation functions were normalized prior to Fourier transformation. Normalization highlights differences in the shapes of the spectral density functions. Non-normalized spectral density functions (Figure 7 inset) account, in addition, for the differences in $G(0)$ magnitudes of the two interactions. Differences in the behavior of cylindrical vs spherical micelles are apparent from these functions, especially at low frequencies. The spectral density for intermolecular interactions is higher for cylindrical than for spherical micelles in the low-frequency region. We cannot extrapolate these curves to frequencies close to zero because we do not have an analytic functional form. Nevertheless, we can conclude that the cylindrical micelle experiences relatively slower modulation of intermolecular 1−2 dipole−dipole interactions. For the intramolecular interactions, the two spectral density functions largely overlap except at a single point at the lowest frequency. This indicates that the correlation function does not decay to zero during the duration of the simulation. Though this residual correlation is not visible to the eye (Figure 6), direct averaging of the tail of the correlation function supports its presence. It follows that the small residual correlation in the correlation function may make an important contribution to the low-frequency spectral density and to the negative cross-relaxation rate observed in cylindrical but not spherical micelles.

Dynamic Analysis of Directly Bonded $^{1}H-^{13}C$ Interactions. For ^{13}C longitudinal relaxation, extraction of spectral density functions leads to the predicted relaxation times listed in Table 2. For this case, we do not need to extrapolate to time scales outside the range directly sampled by the simulations, so it is possible to calculate relaxation rates quantitatively by using a parametrized fitting function that enables smoothing and interpolation. Without implying a mechanistic dynamic model, we describe the correlation functions as sums of four exponential functions. For each exponential component, we include a term $a_i\tau_{c,i}/(1 + \omega^2\tau_{c,i}^2)$ in the spectral density functions, where a_i is the intensity of component i, $\tau_{c,i}$ is the correlation time for component i, and ω refers to the appropriate frequency or sum or difference of frequencies. Using the resulting spectral density functions in eq 6 gives the relaxation times listed in Table 1. Calculated relaxation times are similar for both cylindrical and spherical cases and agree well with the experiment. Taken together, the cross-relaxation and carbon relaxation results indicate that the MD simulations, interpreted without a dynamic model, are consistent with the experiment. In particular, the quantitative agreement of predicted and measured ^{13}C T_1 values gives confidence that the MD simulations are successfully modeling important aspects of the internal dynamics of the micelles.

Effects of Micelle Morphology on Distances and Dynamics. Different micelle morphologies lead to different packing constraints and corresponding differences in dynamics. To explore the packing constraints, Figure 8 shows the numbers of 1−1 spin pairs vs distance for spherical and cylindrical micelles. This gives a measure of the packing density of headgroups in the boundary region of the micelle. The number of spins grows more slowly with spherical micelles compared with cylindrical micelles, showing that the surface density and the total number of coupling partners are smaller in spherical compared with cylindrical micelles. This difference in density is evident even within local (<4.5 Å) distances, emphasizing the additive effects of interacting spins within a fluid.[46]

One common way to characterize aggregate shape with surfactant structure is by the packing parameter $N = v/(a \times l)$. This relates micelle morphology to the volume v per surfactant molecule in the aggregate, the radius l of the aggregate core, and the area a of the headgroup.[2,3] For idealized shapes, this dimensionless parameter, as a direct consequence of geometry, increases in the progression from spherical ($N = 0.33$) to cylindrical ($N = 0.5$) to planar ($N = 1$) structures. Since $C_{12}E_4$ has smaller polar headgroups compared with $C_{12}E_8$, the conversion from spherical to cylindrical shape likely is due to a reduction in a, and this is likely to influence the internuclear distances and dynamics near the hydrophobic−hydrophilic boundary where positions 1 and 2 predominantly reside.

From this simple perspective, it might be expected that the distance distribution among headgroup atoms should be relatable to these geometric descriptors. However, the distance distributions cannot be easily analyzed by assuming that the atoms reside in a thin shell on the surface of a sphere or cylinder because the micelles are not adequately approximated by these shapes and because the position 1 hydrogen atoms do not reside in a thin enough shell.

Nevertheless, it is possible to use the distance distributions to characterize micelle morphology and packing density more fully. Figure 8 shows a graph of the logarithm of the number of atoms vs the logarithm of the distance. Such plots should have a slope equal to $d - 1$, where d is the dimension of the object on the scale indicated by the horizontal axis. An idealized cylindrical shell having a uniform distribution and thickness, for example, would have dimension 3 at distances less than the thickness of the shell. This dimension would decrease to 2 when the distance exceeds the width of the shell but remains less than the radius of the cylinder, and it would decrease

DOI: 10.1021/acs.langmuir.9b01345
Langmuir 2019, 35, 13880−13892

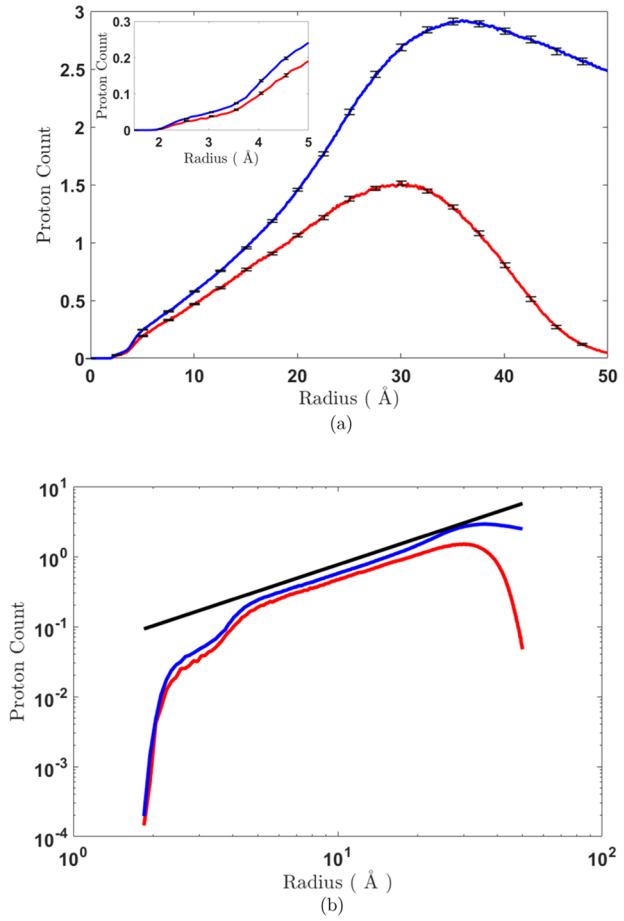

Figure 8. (a) Histogram of intermolecular C1 proton counts as a function of radius. The bin width is 0.1 Å. The red curve corresponds to the spherical micelle, and the blue curve corresponds to the cylindrical micelle. Error bars are shown in black. Inset: close-up of the radius region from 1.5 to 5 Å. Each line corresponds to averages taken over five separate 1.4 ns sections of trajectory for 99 surfactant molecules. For the spherical micelle, this encompasses all surfactant molecules within the micelle. For the cylindrical micelle, this encompasses 99 $C_{12}E_8$ molecules and 99 $C_{12}E_4$ molecules separately. (b) Histograms displayed on a log–log plot, using the same color code as in (a), with a reference line of slope 1.25 shown in black.

further to 1 when the distance is larger than the radius but less than the length of the cylinder. Finally, the dimension would decrease to zero once the distance exceeds the length of the cylinder.

At distances between about 4.5 and 15 Å, which spans a range that is larger than the methylene groups but smaller than the average radii of the aggregates, both curves in Figure 8 inset are roughly linear and have slopes approximating 1.25, indicating a dimension $d \simeq 2.25$. This is indicated by the slope of the black line included for reference. A noninteger dimension somewhat greater than 2 is related to the thickness of the distribution of hydrogen atoms bound to carbon 1 in these aggregates. It is also noteworthy that the curves for spherical and cylindrical micelles are parallel, but the cylindrical micelle curve is displaced upward. This indicates again that the density of type 1 hydrogen atoms is higher in the cylindrical compared with that in the spherical micelles, even though the dimensionality of the region is similar.

Prevalence of Negative Cross-Relaxation Signals in NOESY Spectra. As described above and shown in Figure 4, nearly all of the cross-relaxation rates observed in the NOESY spectra have negative signs, indicating that the zero-frequency spectral density components in eq 5 usually dominate cross-relaxation. We investigate the origin of this by analyzing the MD simulations. We find that the slow motions that accompany this effect are due to large numbers of long-range interactions and that the correlation functions for long-range interactions decay slowly as a consequence of the relatively long distances involved.

Figure 9 shows that even the hydrogen atoms at position 12, which are expected to be among the most mobile atoms in the

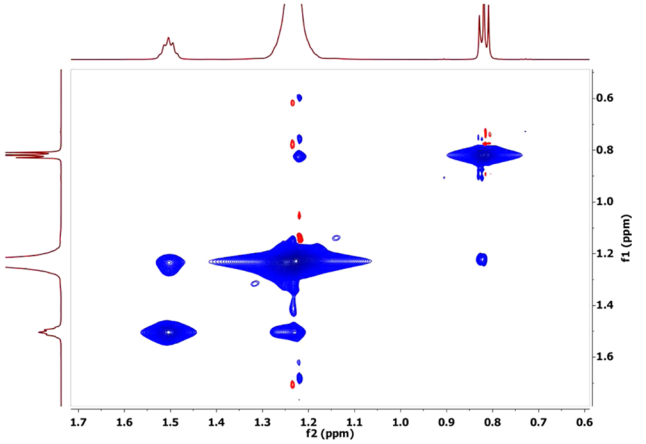

Figure 9. Region of the ^{1}H-^{1}H NOESY spectrum of 80 mM $C_{12}E_8$ in D_2O at 25 °C showing cross-peaks between terminal methyl C12 protons, central alkyl chain protons C3–C11, and C2 protons (for carbon numbering convention, refer to Figure 1). Chemical shifts relevant to the cross-peaks are identified in the one-dimensional ^{1}H spectra displayed along the axes. Diagonal peaks and negative cross-peaks are indicated using blue contours, and red is used for positive contours. Note that all of the cross-peaks are negative.

micelles, exhibit net negative cross-relaxation rates with the bulk of the alkyl chain hydrogen atoms. We expect slower modulations of internuclear vectors for most other pairs of atoms and correspondingly more negative cross-relaxation rates. We therefore consider the dynamics of internuclear vectors involving position 12 in detail as a limiting case. Figure 10 shows spectral density functions derived from the MD simulations that involve hydrogen atoms at position 12. We separately calculate intramolecular and intermolecular spectral density functions because they are subject to very different geometric constraints and therefore exhibit very different relative motions. Because the different classes of interacting atoms are not distinguished spectroscopically, the measured cross-relaxation rates result from a weighted sum of the two types of interactions.

The red and orange curves in Figure 10 characterize modulation of the intramolecular and intermolecular vectors joining positions 12 and 11. For the intramolecular vector, the correlation function decays very quickly, so that the spectral density function is liquidlike, having low intensity at low frequencies. Hence, intramolecular interactions on adjacent positions do not contribute to the negative sign of the cross-relaxation rates. The intermolecular correlation function, on the other hand, decays much more slowly. Although we cannot extrapolate the spectral density function to near-zero frequency because of the finite duration of the simulation, it is apparent that the low-frequency spectral density function is large for the

DOI: 10.1021/acs.langmuir.9b01345
Langmuir 2019, 35, 13880–13892

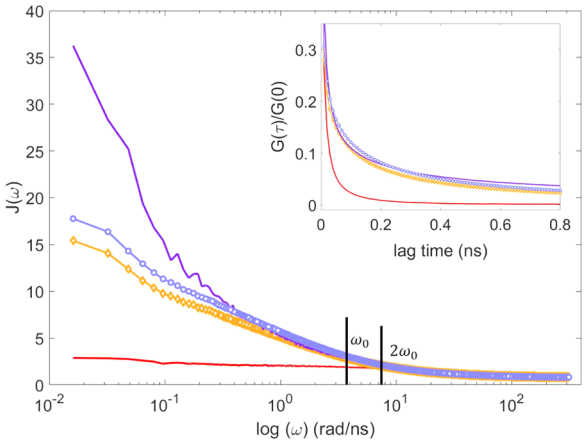

Figure 10. Normalized spectral density functions for intramolecular and intermolecular dipolar interactions involving protons at position 12. For 11−12, intramolecular interactions are indicated with red, and intermolecular interactions are indicated with orange. For 10−12, intramolecular interactions are indicated with blue, and intermolecular interactions are indicated with purple. ω_0 denotes the Larmor frequency. Inset: corresponding normalized correlation functions. The large, low-frequency components are responsible for predominantly negative cross-relaxation rates observed experimentally.

intermolecular interaction. This suggests that the intermolecular interactions lead to a negative cross-relaxation rate.

The blue and purple curves in Figure 10 characterize modulation of the intramolecular and intermolecular vectors joining more distant positions, namely, 12 and 10. Compared with the correlation functions for the 12−11 interaction, the 12−10 correlation functions decay even more slowly. This leads to even larger low-frequency contributions to the spectral density functions and therefore to more negative cross-relaxation rates. As expected from simple geometric considerations, as the distance between atoms is larger, the relative contribution of slow motions to the correlation function increases. When atoms are constrained to reside at long distances, or when they are free to sample predominantly large distances within the aggregate, they are likely to exhibit negative cross-relaxation rates.

SUMMARY AND CONCLUSIONS

NMR relaxation measurements and atomistic MD simulations provide insights into the structure and dynamics of spherical and cylindrical micelles formed by pure and mixed nonionic alkyl ethoxylate surfactants. NMR relaxation results indicate rich internal dynamics with motions occurring over a wide range of time scales. ^{13}C longitudinal relaxation times imply the presence of liquidlike local motions, while two-dimensional cross-relaxation measurements, as indicated by predominantly negative cross-relaxation rates, imply the simultaneous presence of slow motions. In spherical micelles, but not in cylindrical micelles, the cross-relaxation rate linking hydrogen atoms in alkane positions 1 and 2, located near the hydrophilic−hydrophobic boundary, is positive. This implies a relative absence of slow motions in the boundary region of spherical micelles. MD simulations are used to construct correlation functions, spectral density functions, and positional distribution functions that rationalize the experimental results. These functions are calculated directly from the simulations, without fitting to any assumed functional form. Results indicate that relative motions of nearby atoms are liquidlike, in agreement with ^{13}C T_1 measurements, though constrained by micelle morphology. Relative motions of distant atoms have slower components because the relative changes in distances and angles are smaller when the moving atoms are further apart. The slow, long-range motions appear to be responsible for the predominantly negative cross-relaxation rates observed in NOESY spectra. The densities of atoms from positions 1 and 2 in the boundary region are lower in spherical micelles compared with cylindrical micelles. Correspondingly, motions in this region are less constrained by micelle morphology in the spherical compared with the cylindrical cases. The two effects of morphology lead to the unusual occurrence of positive cross-relaxation involving positions 1 and 2 for spheres.

ASSOCIATED CONTENT

Supporting Information

The Supporting Information is available free of charge on the ACS Publications website at DOI: 10.1021/acs.langmuir.9b01345.

^1H-^1H NOESY spectrum of 80 mM $C_{12}E_8$ in D_2O at 25 °C; ^1H-^1H NOESY spectrum of equimolar mixture of 40 mM $C_{12}E_8$ 40 mM $C_{12}E_4$ in D_2O at 25°C (PDF)

AUTHOR INFORMATION

Corresponding Authors

*E-mail: george.stan@uc.edu. Phone: +1 (513) 556-3049. Fax: +1 (513) 556-9239 (G.S.).

*E-mail: eads.cd@pg.com. Phone: +1 (513) 526-9388 (C.D.E.).

ORCID

George Stan: 0000-0003-1880-4173

Present Address

‖Discovery, Product Development Supply, Janssen Research & Development, Spring House, Pennsylvania 19477, United States (A.J.).

Notes

The authors declare no competing financial interest.

ACKNOWLEDGMENTS

The authors thank Rafael Brüschweiler, Rich Pastor, Peter Koenig, and David Eike for insightful discussion. This work has been supported in part by the National Science Foundation (NSF) grant MCB-1516918 to G.S. This work used resources of the Oak Ridge Leadership Computing Facility, which is a DOE Office of Science User Facility supported under Contract DE-AC05-00OR22725 through Project CHP105 to A.T.E. Portions of this work benefited from and provided support to the NIST nSoft consortium (www.nist.gov/nsoft), including use of the 10 m Small Angle Neutron Scattering instrument at the NCNR. This work benefited from the use of the SasView application, originally developed under NSF Award DMR-0520547. SasView also contains a code developed with funding from the EU Horizon 2020 program under the SINE2020 project Grant no. 654000. Commercial products identified in this manuscript are included for the purpose of including a complete and accurate description of the methods and materials used in this work and are not an endorsement by the National Institute of Standards and Technology.

DOI: 10.1021/acs.langmuir.9b01345
Langmuir 2019, 35, 13880−13892

REFERENCES

(1) Laughlin, R. G. *The Aqueous Phase Behavior of Surfactants*, 1st ed.; Academic Press, Inc.: San Diego, 1994.
(2) Israelachvili, J. N. *Intermolecular and Surface Forces*, 3rd ed.; Elsevier Inc.: New York, 2011.
(3) Holmberg, K.; Jönsson, B.; Kronberg, B.; Lindman, B. *Surfactants and Polymers in Aqueous Solution*, 2nd ed.; John Wiley & Sons: Norfolk, U.K., 2007.
(4) Terrón-Mejiá Ketzasmin, A.; López-Rendón, R.; Goicochea, A. G. Desorption of hydrocarbon chains by association with ionic and nonionic surfactants under flow as a mechanism for enhanced oil recovery. *Sci. Rep.* **2017**, *7*, No. 9586.
(5) Kuramochi, H.; Andoh, Y.; Yoshii, N.; Okazaki, S. All-Atom Molecular Dynamics Study of a Spherical Micelle Composed of N-Acetylated Poly (ethylene glycol)-Poly (γ-benzyl L -glutamate) Block Copolymers: A Potential Carrier of Drug Delivery Systems for Cancer. *J. Phys. Chem. B* **2009**, *113*, 15181−15188.
(6) Callari, M.; DeSouza, P. L.; Rawal, A.; Stenzel, M. H. The Effect of Drug Loading on Micelle Properties: Solid-State NMR as a Tool to Gain Structural Insight. *Angew. Chem., Int. Ed.* **2017**, *56*, 8441−8445.
(7) Cates, M. E.; Candau, S. J. Statics and dynamics of worm-like surfactant micelles. *J. Phys.: Condens. Matter* **1990**, *2*, 6869−6892.
(8) Berret, J.-F.; Appell, J.; Porte, G. Linear Rheology of Entangled Wormlike Micelles. *Langmuir* **1993**, *9*, 2851−2854.
(9) Lin, Z.; Eads, C. D. Polymer-Induced Structural Transitions in Oleate Solutions: Microscopy, Rheology, and Nuclear Magnetic Resonance Studies. *Langmuir* **1997**, *13*, 2647−2654.
(10) Einaga, Y. Wormlike Micelles of Polyoxyethylene Alkyl Ethers C_iE_j. *Polym. J.* **2009**, *41*, 157−173.
(11) Osei-Bonsu, K.; Shokri, N.; Grassia, P. Foam stability in the presence and absence of hydrocarbons: From bubble- to bulk-scale. *Colloids Surf., A* **2015**, *481*, 514−526.
(12) Tang, X.; Zou, W.; Koenig, P. H.; McConaughy, S. D.; Weaver, M. R.; Eike, D. M.; Schmidt, M. J.; Larson, R. G. Multiscale Modeling of the Effects of Salt and Perfume Raw Materials on the Rheological Properties of Commercial Threadlike Micellar Solutions. *J. Phys. Chem. B* **2017**, *121*, 2468−2485.
(13) Penfold, J.; Tucker, I.; Green, A.; Grainger, D.; Jones, C.; Ford, G.; Roberts, C.; Hubbard, J.; Petkov, J.; Thomas, R. K.; Grillo, I. Impact of Model Perfumes on Surfactant and Mixed Surfactant Self-Assembly. *Langmuir* **2008**, *24*, 12209−12220.
(14) Bradbury, R.; Penfold, J.; Thomas, R. K.; Tucker, I. M.; Petkov, J. T.; Jones, C.; Grillo, I. Impact of Model Perfume Molecules on the Self-Assembly of Anionic Surfactant Sodium Dodecyl 6-Benzene Sulfonate. *Langmuir* **2013**, *29*, 3234−3245.
(15) Fischer, E.; Fieber, W.; Navarro, C.; Sommer, H.; Benczédi, D.; Velazco, M. I.; Schönhoff, M. Partitioning and Localization of Fragrances in Surfactant Mixed Micelles. *J. Surfactants Deterg.* **2009**, *12*, 73−84.
(16) Rangel-Yagui, C. O.; Pessoa, A., Jr; Tavares, L. C. Micellar solubilization of drugs. *J. Pharm. Pharm. Sci.* **2005**, *8*, 147−163.
(17) Kunieda, H.; Ozawa, K.; Huang, K.-L. Effect of Oil on the Surfactant Molecular Curvatures in Liquid Crystals. *J. Phys. Chem. B* **1998**, *102*, 831−838.
(18) Liu, Q.; Ji, X.; Wang, S.; Zou, W.; Li, J.; Lv, D.; Yin, B.; Yan, H.; Wei, X. Effect of Additives on Surfactant Micelle Shape Transformation: Rheology and Molecular Dynamics Studies. *J. Phys. Chem. C* **2019**, *123*, 2922−2932.
(19) Kaizu, K.; Alexandridis, P. Glucose-induced sphere to ellipsoid transition of polyoxyethylene - polyoxypropylene block copolymer micelles in aqueous solutions. *Colloids Surf., A* **2015**, *480*, 203−213.
(20) Yoshii, N.; Nimura, Y.; Fujimoto, K.; Okazaki, S. Spherical harmonics analysis of surface density fluctuations of spherical ionic SDS and nonionic $C_{12}E_8$ micelles: A molecular dynamics study. *J. Chem. Phys.* **2017**, *147*, No. 034906.
(21) Yuan, F.; Wang, S.; Larson, R. G. Potentials of mean force and escape times of surfactants from micelles and hydrophobic surfaces using molecular dynamics simulations. *Langmuir* **2015**, *31*, 1336−1343.
(22) Braun, D.; Steinhauser, O. The intermolecular NOE is strongly influenced by dynamics. *Phys. Chem. Chem. Phys.* **2015**, *17*, 8509−8517.
(23) Gujt, J.; Bešter-Rogač, M.; Spohr, E. Structure and Stability of Long Rod-like Dodecyltrimethylammonium Chloride Micelles in Solutions of Hydroxybenzoates: A Molecular Dynamics Simulation Study. *Langmuir* **2016**, *32*, 8275−8286.
(24) Ferreira, T. M.; Medronho, B.; Martin, R. W.; Topgaard, D. Segmental order parameters in a nonionic surfactant lamellar phase studied with ^{1}H-^{13}C solid-state NMR. *Phys. Chem. Chem. Phys.* **2008**, *10*, 6033−6038.
(25) Padia, F. N.; Yaseen, M.; Gore, B.; Rogers, S.; Bell, G.; Lu, J. R. Influence of Molecular Structure on the Size, Shape, and Nanostructure of Nonionic C_nE_m Surfactant Micelles. *J. Phys. Chem. B* **2014**, *118*, 179−188.
(26) Dixon, A. M.; Venable, R. M.; Pastor, R. W.; Bull, T. E. Micelle-bound conformation of a hairpin-forming peptide: Combined NMR and molecular dynamics study. *Biopolymers* **2002**, *65*, 284−298.
(27) Shintani, M.; Yoshida, K.; Sakuraba, S.; Nakahara, M.; Matubayasi, N. NMR-NOE and MD Simulation Study on Phospholipid Membranes: Dependence on Membrane Diameter and Multiple Time Scale Dynamics. *J. Phys. Chem. B* **2011**, *115*, 9106−9115.
(28) Cao, C.; Mao, J.; Li, F.; Yang, M.; He, H.; Jiang, L.; Liu, M. Understanding the Interaction between Valsartan and Detergents by NMR Techniques and Molecular Dynamics Simulation. *J. Phys. Chem. B* **2012**, *116*, 7470−7478.
(29) Ferreira, T. M.; Topgaard, D.; Ollila, O. H. S. Molecular Conformation and Bilayer Pores in a Nonionic Surfactant Lamellar Phase Studied with ^{1}H-^{13}C Solid-State NMR and Molecular Dynamics Simulations. *Langmuir* **2014**, *30*, 461−469.
(30) Kimmich, R.; Fatkullin, N. Self-diffusion studies by intra- and inter-molecular spin-lattice relaxometry using field-cycling: Liquids, plastic crystals, porous media, and polymer segments. *Prog. Nucl. Magn. Reson. Spectrosc.* **2017**, *101*, 18−50.
(31) Wachowicz, M.; Jurga, S.; Vilfan, M. Collective and local molecular dynamics in the lyotropic mesophases of decylammonium chloride: ^{1}H and ^{2}H NMR study. *Phys. Rev. E* **2004**, *70*, No. 031701.
(32) Yang, Q.; Zhou, Q.; Somasundaran, P. Mixed micelles of octane-1,8 bis(dodecyl dimethyl ammonium chloride) and n-dodecyl-β-d-maltoside by ^{1}H NMR study. *Colloids Surf., A* **2007**, *305*, 22−28.
(33) Peter, C.; Daura, X.; Gunsteren, W. F. Calculation of NMR-relaxation parameters for exible molecules from molecular dynamics simulations. *J. Biomol. NMR* **2001**, *20*, 297−310.
(34) Wennerstroem, H.; Lindman, B.; Söderman, O.; Drakenberg, T.; Rosenholm, J. B. ^{13}C Magnetic Relaxation in Micellar Solutions. Influence of Aggregate Motion on T1. *J. Am. Chem. Soc.* **1979**, *101*, 6860−6864.
(35) Néry, H.; Söderman, O.; Canet, D.; Walderhaug, H.; Lindman, B. Surfactant dynamics in spherical and nonspherical micelles. A nuclear magnetic resonance study. *J. Phys. Chem. A.* **1986**, *90*, 5802−5808.
(36) Ribeiro, A. A.; Dennis, E. A. A Carbon-13 and Proton Nuclear Magnetic Resonance Study on the Structure and Mobility of Nonionic Alkyl Polyoxyethylene Ether Micelles. *J. Phys. Chem. A.* **1977**, *81*, 957−963.
(37) Brüschweiler, R.; Case, D. A. Characterization of biomolecular structure and dynamics by NMR cross relaxation. *Prog. Nucl. Magn. Reson. Spectrosc.* **1994**, *26*, 27−58.
(38) MacKerell, A. D., Jr Molecular Dynamics Simulation Analysis of a Sodium Dodecyl Sulfate Micelle in Aqueous Solution: Decreased Fluidity of the Micelle Hydrocarbon Interior. *J. Phys. Chem. A.* **1995**, *99*, 1846−1855.
(39) Tieleman, D. P.; van der Spoel, D.; Berendsen, H. J. C. Molecular Dynamics Simulations of Dodecylphosphocholine Micelles at Three Different Aggregate Sizes: Micellar Structure and Chain Relaxation. *J. Phys. Chem. B* **2000**, *104*, 6380−6388.

DOI: 10.1021/acs.langmuir.9b01345
Langmuir 2019, 35, 13880−13892

(40) Bogusz, S.; Venable, R. M.; Pastor, R. W. Molecular dynamics simulations of octyl glucoside micelles: Dynamic properties. *J. Phys. Chem. B* **2001**, *105*, 8312−8321.
(41) Denham, N.; Holmes, M. C.; Zvelindovsky, A. V. The Phases in a Non-Ionic Surfactant ($C_{12}E_6$) - Water Ternary System: A Coarse-Grained Computer Simulation. *J. Phys. Chem. B* **2011**, *115*, 1385−1393.
(42) Galiullina, L. F.; Rakhmatullin, I. Z.; Klochkova, E. A.; Aganov, A. V.; Klochkov, V. V. Structure of pravastatin and its complex with sodium dodecyl sulfate micelles studied by NMR spectroscopy. *Magn. Reson. Chem.* **2014**, *53*, 110−114.
(43) Ferreira, T. M.; Ollila, O. H. S.; Pigliapochi, R.; Dabkowska, A. P.; Topgaard, D. Model-free estimation of the effective correlation time for C-H bond reorientation in amphiphilic bilayers: ^{1}H-^{13}C solid-state NMR and MD simulations. *J. Chem. Phys.* **2015**, *142*, No. 044905.
(44) Singer, P. M.; Asthagiri, D.; Chapman, W. G.; Hirasaki, G. J. Molecular dynamics simulations of NMR relaxation and diffusion of bulk hydrocarbons and water. *J. Magn. Reson.* **2017**, *277*, 15−24.
(45) Torrey, H. C. Bloch Equations with Diffusion Terms. *Phys. Rev.* **1956**, *104*, 563−565.
(46) Halle, B. Cross-relaxation between macromolecular and solvent spins: The role of long-range dipole couplings. *J. Chem. Phys.* **2003**, *119*, 12372−12385.
(47) Gabl, S.; Schröder, C.; Braun, D.; Weingärtner, H.; Steinhauser, O. Pair dynamics and the intermolecular nuclear Overhauser effect (NOE) in liquids analysed by simulation and model theories: Application to an ionic liquid. *J. Chem. Phys.* **2014**, *140*, No. 184503.
(48) Mitchell, D. J.; Tiddy, G. J. T.; Waring, L.; Bostock, T.; McDonald, M. P. Phase Behaviour of Polyoxyethylene Surfactants with Water. *J. Chem. Soc., Faraday Trans. 1* **1983**, *79*, 975−1000.
(49) Nilsson, P. G.; Wennerström, H.; Lindman, B. Structure of micellar solutions of nonionic surfactants. Nuclear magnetic resonance self-diffusion and proton relaxation studies of poly(ethylene oxide) alkyl ethers. *J. Phys. Chem. A.* **1983**, *87*, 1377−1385.
(50) Tse-Ve-Koon, K.; Tremblay, N.; Constantin, D.; Freyssingeas, É. Structure, thermodynamics and dynamics of the isotropic phase of spherical non-ionic surfactant micelles. *J. Colloid Interface Sci.* **2013**, *393*, 161−173.
(51) Velinova, M.; Sengupta, D.; Tadjer, A. V.; Marrink, S. J. Sphere-to-Rod Transitions of Nonionic Surfactant Micelles in Aqueous Solution Modeled by Molecular Dynamics Simulations. *Langmuir* **2011**, *27*, 14071−14077.
(52) Sterpone, F.; Briganti, G.; Pierleoni, C. Molecular Dynamics Study of Spherical Aggregates of Chain Molecules at Different Degrees of Hydrophilicity in Water Solution. *Langmuir* **2001**, *17*, 5103−5110.
(53) Bernheim-Groswasser, A.; Wachtel, E.; Talmon, Y. Micellar Growth, Network Formation, and Criticality in Aqueous Solutions of the Nonionic Surfactant $C_{12}E_5$. *Langmuir* **2000**, *16*, 4131−4140.
(54) Thomas, H. G.; Lomakin, A.; Blankschtein, D.; Benedek, G. B. Growth of Mixed Nonionic Micelles. *Langmuir* **1997**, *13*, 209−218.
(55) Ahlnaes, T.; Karlström, G.; Lindman, B. Dynamics and Order of Nonionic Surfactants in Neat Liquid and Micellar Solution from Multifield ^{13}C NMR Relaxation and ^{13}C NMR Chemical Shifts. *J. Phys. Chem. A.* **1987**, *91*, 4030−4036.
(56) Matsumoto, T.; Zenkoh, H. Micelle structure in isotropic aqueous colloids of a poly(oxyethylene) amphiphile $C_{12}E_8$. *Colloid Polym. Sci.* **1990**, *268*, 536−543.
(57) Sterpone, F.; Briganti, G.; Pierleoni, C. Sphere versus Cylinder: The Effect of Packing on the Structure of Nonionic $C_{12}E_6$ Micelles. *Langmuir* **2009**, *25*, 8960−8967.
(58) Aoun, B.; Sharma, V. K.; Pellegrini, E.; Mitra, S.; Johnson, M.; Mukhopadhyay, R. Structure and dynamics of ionic micelles: MD simulation and neutron scattering study. *J. Phys. Chem. B* **2015**, *119*, 5079−5086.
(59) Degiorgio, V.; Piazza, R.; Corti, M.; Minero, C. Critical properties of nonionic micellar solutions. *J. Chem. Phys.* **1985**, *82*, 1025−1031.
(60) Magid, L. J.; Triolo, L. R.; Caponetti, E.; Johnson, J. S., Jr *Surfactants in Solution*; Mittal, K. L.; Lindman, B., Eds.; Plenum Press: New York, 1986; pp 155−178.
(61) Tanford, C.; Nozakl, Y.; Rohde, M. F. Size and Shape of Globular Micelles Formed in Aqueous Solution by n-Alkyl Polyoxyethylene Ethers. *J. Phys. Chem. A.* **1977**, *81*, 1555−1560.
(62) Zana, R.; Lévy, H.; Kwetkat, K. Mixed micellization of dimeric (gemini) surfactants and conventional surfactants. I. Mixtures of an anionic dimeric surfactant and of the nonionic surfactants $C_{12}E_5$ and $C_{12}E_8$. *J. Colloid Interface Sci.* **1998**, *197*, 370−376.
(63) Jerke, G.; Pedersen, J. S.; Egelhaaf, S. U.; Schurtenberger, P. Flexibility of Charged and Uncharged Polymer-like Micelles. *Langmuir* **1998**, *14*, 6013−6024.
(64) Martínez, L.; Andrade, R.; Birgin, E. G.; Martínez, J. Packmol: A Package for Building Initial Configurations for Molecular Dynamics Simulations. *J. Comput. Chem.* **2009**, *30*, 2157−2164.
(65) Phillips, J. C.; Braun, R.; Wang, W.; Gumbart, J.; Tajkhorshid, E.; Villa, E.; Chipot, C.; Skeel, R. D.; Kalé, L.; Schulten, K. Scalable molecular dynamics with NAMD. *J. Comput. Chem.* **2005**, *26*, 1781−1802.
(66) Best, R. B.; Zhu, X.; Shim, J.; Lopes, P. E. M.; Mittal, J.; Feig, M.; MacKerell, A. D., Jr Optimization of the additive CHARMM all-atom protein force field targeting improved sampling of the backbone ϕ, ψ and sidechain $\chi1$ and $\chi2$ dihedral angles. *J. Chem. Theory Comput.* **2012**, *8*, 3257−3273.
(67) Huang, J.; Rauscher, S.; Nawrocki, G.; Ran, T.; Feig, M.; de Groot, B. L.; Grubmüller, H.; MacKerell, A. D., Jr CHARMM36m: An Improved Force Field for Folded and Intrinsically Disordered Proteins. *Nat. Methods* **2017**, *14*, 71−73.
(68) Lee, H.; Venable, R. M.; MacKerell, A. D., Jr; Pastor, R. W. Molecular Dynamics Studies of Polyethylene Oxide and Polyethylene Glycol: Hydrodynamic Radius and Shape Anisotropy. *Biophys. J.* **2008**, *95*, 1590−1599.
(69) Tang, X.; Koenig, P. H.; Larson, R. G. Molecular dynamics simulations of sodium dodecyl sulfate micelles in water - The effect of the force field. *J. Phys. Chem. B* **2014**, *118*, 3864−3880.
(70) Eismin, R. J.; Munusamy, E.; Kegel, L. L.; Hogan, D. E.; Maier, R. M.; Schwartz, S. D.; Pemberton, J. E. Evolution of Aggregate Structure in Solutions of Anionic Monorhamnolipids: Experimental and Computational Results. *Langmuir* **2017**, *33*, 7412−7424.
(71) Luft, C. M.; Munusamy, E.; Pemberton, J. E.; Schwartz, S. D. Molecular Dynamics Simulation of the Oil Sequestration Properties of a Nonionic Rhamnolipid. *J. Phys. Chem. B* **2018**, *122*, 3944−3952.
(72) Essmann, U.; Perera, L.; Berkowitz, M. L.; Darden, T.; Lee, H.; Pedersen, L. G. A smooth particle mesh Ewald method. *J. Chem. Phys.* **1995**, *103*, 8577−8593.
(73) Ryckaert, J. P.; Ciccotti, G.; Berendsen, H. J. C. Numerical integration of the cartesian equations of motion of a system with constraints: molecular dynamics of n-alkanes. *J. Comp. Phys.* **1977**, *23*, 327−341.
(74) Salaniwal, S.; Cui, S. T.; Cochran, H. D.; Cummings, P. T. Molecular simulation of a dichain surfactant/water/carbon dioxide system. 2. Self-Assembly and Aggregation Dynamics. *Langmuir* **2001**, *17*, 1784−1792.
(75) Abragam, A. *The Principles of Nuclear Magnetism*, 1st ed.; Oxford University Press: London, 1961.
(76) Ernst, R. R.; Bodenhausen, G.; Wokaun, A. *Principles of Nuclear Magnetic Resonance in One and Two Dimensions*, 1st ed.; Clarendon Press, 1987.
(77) Kowalewski, J.; Mäler, L. *Nuclear Spin Relaxation in Liquids: Theory, Experiments, and Applications*, 1st ed.; Moore, J.; Spencer, N., Eds.; Taylor & Francis Group, LLC: Boca Raton, FL, 2006.
(78) Cowan, B. *Nuclear Magnetic Resonance and Relaxation*, 1st ed.; Cambridge University Press: New York, 1997; p 434.
(79) Bloembergen, N.; Purcell, E. M.; Pound, R. V. Relaxation effects in nuclear magnetic resonance absorption. *Phys. Rev.* **1948**, *73*, 679−712.

DOI: 10.1021/acs.langmuir.9b01345
Langmuir 2019, 35, 13880−13892

(80) Ollila, O. H. S.; Heikkinen, H. A.; Iwaï, H. Rotational Dynamics of Proteins from Spin Relaxation Times and Molecular Dynamics Simulations. *J. Phys. Chem. B* **2018**, *122*, 6559−6569.
(81) Klauda, J. B.; Roberts, M. F.; Redfield, A. G.; Brooks, B. R.; Pastor, R. W. Rotation of Lipids in Membranes: Molecular Dynamics Simulation, ^{31}P Spin-Lattice Relaxation, and Rigid-Body Dynamics. *Biophys. J.* **2008**, *94*, 3074−3083.
(82) Halle, B.; Wennerström, H. Interpretation of magnetic resonance data from water nuclei in heterogeneous systems. *J. Chem. Phys.* **1981**, *75*, 1928−1943.
(83) Macura, S.; Ernst, R. Elucidation of cross relaxation in liquids by two-dimensional N.M.R. spectroscopy. *Mol. Phys.* **1980**, *41*, 95−117.
(84) Kline, S. R. Reduction and analysis of SANS and USANS data using IGOR Pro. *J. Appl. Crystallogr.* **2006**, *39*, 895−900.
(85) Guinier, A.; Fournet, G. *Small-Angle Scattering of X-Rays*; John Wiley & Sons: New York, 1955.
(86) Pedersen, J. S. Analysis of small-angle scattering data from colloids and polymer solutions: modeling and least-squares fitting. *Adv. Colloid Interface Sci.* **1997**, *70*, 171−210.
(87) Doucet, M., et al.et al. *SasView* Version 4.1; Zenodo: 2017; DOI: 10.5281/zenodo.438138.
(88) Neuhaus, D.; Williamson, M. P. *The Nuclear Overhauser Effect in Structural and Conformational Analysis*, 1st ed.; VCH Publishers, Inc.: New York, 1989.
(89) Balmbra, R. R.; Clunie, J. S.; Corkill, J. M.; Goodman, J. F. Effect of Temperature on the Micelle Size of a Homogeneous Non-ionic Detergent. *J. Chem. Soc., Faraday Trans.* **1962**, *58*, 1661−1667.

DOI: 10.1021/acs.langmuir.9b01345
Langmuir 2019, 35, 13880−13892